GJI Geodesy, potential field and applied geophysics

The effective elastic thickness of the India Plate from receiver function imaging, gravity anomalies and thermomechanical modelling

György Hetényi,[1] Rodolphe Cattin,[1] Jérôme Vergne[1] and John L. Nábělek[2]

[1]*Laboratoire de Géologie, ENS Paris,* 24 *rue Lhomond,* 75005 *Paris, France. E-mail: hetenyi@geologie.ens.fr*
[2]*College of Oceanic and Atmospheric Sciences, Oregon State University, Corvallis,* OR 97331*, USA*

SUMMARY

The range and the meaning of the effective elastic thickness (EET) in continental areas have been subject to controversy over the last two decades. Here we take advantage of the new data set from the Hi-CLIMB seismological experiment to re-estimate the EET of the India Plate along a south–north profile extending from the Ganges basin to central Tibet. Receiver functions give a high-resolution image of the base of the foreland basin at ∼5 km depth and constrain the crustal thickness, which increases northwards from ∼35 km beneath the indo-gangetic plain to ∼70 km in southern Tibet. Together with available data sets including seismic profiles, seismological images from both INDEPTH and HIMNT experiments, deep well measurements and Bouguer anomaly profiles, we interpret this new image with 2-D thermomechanical modelling solutions, using different type of crustal and mantle rheologies. We find that (1) the EET of the India Plate decreases northwards from 60–80 to 20–30 km as it is flexed down beneath Himalaya and Tibet, due to thermal and flexural weakening; (2) the only resistant layer of the India Plate beneath southern Tibet is the upper mantle, which serves as a support for the topographic load and (3) the most abrupt drop in the EET, located around 200 km south of the MFT, is associated with a gradual decoupling between the crust and the mantle. We show that our geometrical constraints do not allow to determine if the upper and lower crust are coupled or not. Our results clearly reveal that a rheology with a weak mantle is unable to explain the geometry of the lithosphere in this region, and they are in favour of a rheology in which the mantle is strong.

Key words: flexure of the lithosphere, gravity anomaly, Himalaya, rheology, *P* waves, *S* waves.

1 INTRODUCTION

The effective elastic thickness (EET) is a concept related to the apparent strength of a plate. Its value over oceanic lithospheres is often associated with the 600 °C isotherm (Burov & Diament 1995; Watts & Zhong 2000). Over continental plates, the estimate of the EET has been subject to controversy and to some more detailed discussion over the last two decades. One of the most discussed regions, despite the extensive studies and large available data sets, is the northern edge of the India–Australia plate (India Plate hereinafter) across the Himalayan belt and Tibet.

Table 1 summarizes the estimates of the EET in the Himalayan-Tibetan region. The first approach was based on the physical equations describing the flexure of a completely elastic beam (Hetényi 1946). As more geophysical data became available (such as gravity anomaly, seismicity, etc.), and more sophisticated modelling tools were developed, the complexity of the models evolved, and several different values have been published for the EET. In the last five years, the debate on the EET concentrated around two school

of thoughts with different views of the rheology: one with a weak mantle and a strong crust (also dubbed 'crème brûlée' by Burov & Watts 2006), and one with a strong mantle and a strong upper crust (also dubbed 'jelly sandwich' by Jackson 2002).

One reason for these uncertainties in the estimate of the EET of the India plate is the lack of continuous information on the shape of its flexure from India to Tibet. In order to investigate the geometry of the lithospheric structures in this area, several seismological experiments were performed, including the HIMNT experiment in Nepal and Southern Tibet (Schulte-Pelkum *et al.* 2005) and the INDEPTH experiment in Tibet (e.g. Zhao *et al.* 1993; Nelson *et al.* 1996; Hauck *et al.* 1998; Alsdorf *et al.* 1998). However, due to the long distance (∼250 km) between HIMNT and INDEPTH experiments, data from these previous results cannot be easily combined. Moreover, these experiments do not extend into the Ganges basin, where a good estimate of the basin and Moho depth are of great importance to evaluate the EET. Here, we take advantage of the new data set from the Hi-CLIMB broad-band seismological experiment, which provides the first detailed and continuous lithospheric profile

Table 1. Summary of the previous estimates of the EET in the Himalayan-Tibetan region by different methods and authors.

EET (km)	Method or concept	Authors
80–110	Elastic plate, Bouguer anomaly	Lyon-Caen & Molnar (1983) Karner & Watts (1983)
90 India 30–45 Tibet	Bouguer anomaly, Variable EET	Jin *et al.* (1996)
42	Free-air anomaly and topography coherence	McKenzie & Fairhead (1997)
40–50 India 30 Tibet	Thermomechanical modelling, Viscoelastoplastic rheology	Cattin *et al.* (2001)
36.5	Seismogenic and elastic thickness similarity ('crème brûlée')	Jackson (2002); based also on Maggi *et al.* (2000)
60–70	Integrated brittle, elastic and ductile strength ('jelly-sandwich')	Watts & Burov (2003); Burov & Watts (2006)

across the Himalayan range, from the Ganges basin to central Tibet (Nábělek *et al.* 2005).

In a first part, we constrain the geometry of the lithospheric structures at two different scales. Using the receiver function method, we image the geometry of the flexural sedimentary foreland basin from

a subset of the new, high-resolution seismological Hi-CLIMB data (Fig. 1, inset). As receiver functions observed in young sedimentary basins have particular properties, we describe our proceedings in detail. At larger scale, we combine the profile up to central Tibet, obtained from more Hi-CLIMB data (Nábělek *et al.* 2005), with
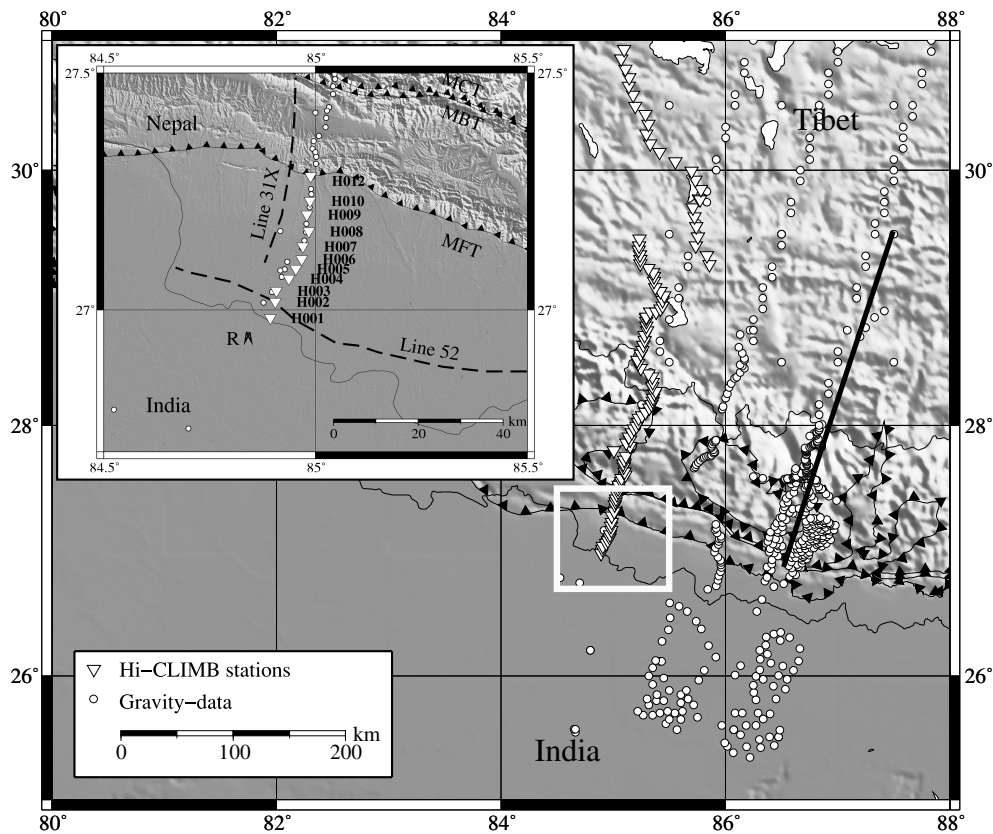

Figure 1. The study-area in northern India, central Nepal and southern Tibet, showing the location of seismological stations (white triangles), gravity measurements (circles) and major thrust-faults. Thick line represents the profile of Schulte-Pelkum *et al.* (2005). Inset: close-up on the northern edge of the Ganges basin and the seismological stations used in this study. Thrust-faults from north to south are the Main Central Thrust (MCT), the Main Boundary Thrust (MBT) and the Main Frontal Thrust (MFT), respectively. 'R' represents deep well data location at Raxaul. Lines 31X and 52 give the location of the seismic reflection profiles mentioned in this study.

previous results from seismic reflection (Zhao *et al.* 1993; Alsdorf *et al.* 1998), receiver function (Hauck *et al.* 1998; Kumar *et al.* 2001; Schulte-Pelkum *et al.* 2005) and gravity anomaly data (Cattin *et al.* 2001).

These sets of information are used in the second part of this study, which focuses on thermomechanical modelling of the flexure of the India Plate under a load representing the Tibetan crust. A large number of parameters are varied, and the results are evaluated upon the aforementioned geometrical criteria. The aim of this study is to demonstrate the consistency of all available geophysical observations, and to re-estimate of the EET and its variation along a profile perpendicular to the mountain range. The validity of the obtained models is tested by calculating the corresponding Bouguer anomaly, and by comparing it with the observations in the same area (Fig. 1; Cattin *et al.* 2001). At the end of this paper, special emphasis is given to the analysis of the time-dependence of the EET.

2 GEODYNAMIC SETTING AND CONSTRAINTS ON THE GEOMETRY OF THE GANGES BASIN

The important amount of shortening that occurred over the last tens of million years (e.g. Lyon-Caen & Molnar 1983; Armijo *et al.* 1986) and continues today (Larson *et al.* 1999; Chen & Yang 2004) between India and Eurasia is mainly accommodated along major thrust faults such as the Main Central Thrust (MCT), the Main Boundary Thrust (MBT) and the Main Frontal Thrust (MFT) (Fig. 1, inset; e.g. Avouac 2003). These faults are thought to root along the Main Himalayan Thrust (MHT), imaged at a depth of 25 to 40 km from the INDEPTH experiment (Zhao *et al.* 1993; Alsdorf *et al.* 1998), which is considered as the plate interface. The MFT is probably the major active fault at present in the Himalaya of central Nepal (Lavé & Avouac 2000). This fault separates the deformed foothills to the north from the underformed foreland basin of the Ganges River to the south. The Raxaul deep well (Fig. 1 inset) reveals the local stratigraphy of the basin showing recent alluvial layers over the molassic Siwaliks Group formation with a total thickness of 4.1 km (Sastri *et al.* 1971). The Siwaliks have three lithostratigraphic units, corresponding to the change in facies from distal mudstone and clay to proximal conglomerate and breccia (Schelling 1992; Métivier *et al.* 1999). The thickness of the alluvial layer may reach up to 1 km and is characterized by very low velocities due to its recent formation and small compaction (Raiverman *et al.* 1983). Seismic reflection profiles designed for commercial exploration are also available (DMG 1990) and, although being of poor quality, provide additional information about the subsurface structures. They seem to indicate that the base of the Ganges basin is essentially flat, both parallel (line 52, Fig. 1, inset) and perpendicular to the Himalayan front (line 31X). The fact that the available profiles are not depth-converted using a laterally varying velocity model precludes more precise dip estimates. Other dip estimates based on gravity anomaly measurements (e.g. Lyon-Caen & Molnar 1983; Cattin *et al.* 2001), on the interpretation of another seismic profile (Lavé & Avouac 2000), and on an aeromagnetic survey (Agocs 1957), rather show a gentle northward deepening of this surface, with dip values ranging between 1.5 and 4°.

A better constrained estimate of the dip of the base of the basin is important, as it is a good indicator of the shape of the flexure of the India Plate, which is dependent of its EET. Measurements of the depth and dip of the base of the basin can thus help to better constrain the EET: a more rigid plate will have a smaller dip, and a less rigid plate a steeper dip.

3 GEOMETRY OF THE STRUCTURES

3.1 The Ganges foreland basin

3.1.1 Seismological data processing

This study is among the firsts that images shallow structures by the mean of high-frequency receiver functions, originally designed to image deeper lithospheric structures (see also Wilson *et al.* (2003) and Zheng *et al.* (2005) for other examples). This technique is aimed to isolate *P*-to-*S* converted waves and multiple reflections/conversions from interfaces associated with an impedance contrast. For the principles, we refer to the works of Langston (1979), Ammon *et al.* (1990) and Ammon (1991). Receiver functions obtained at stations located above young sedimentary cover usually exhibit a very different shape than those located on bedrock, due to contamination by multiple reverberations inside the basin. However, detailed examination and modelling of these receiver functions at high frequency can provide valuable information about the basin structure. Obtaining the correct depth–velocity structure of the basin is also very important to get an accurate estimate of the Moho depth in this region. Neglecting the effect of the basin would lead to an error of several kilometres on the Moho depth.

Here we use 11 three-component broad-band seismological stations of the Hi-CLIMB experiment located in the northern part of the Ganges basin. With the use of receiver functions, we obtain a high-resolution image of the basin structure and an estimate of the Moho depth. The stations were placed at slightly elevated areas above the water table. As insurance from flooding during the monsoon, the seismometers were placed in sealed drums, but there was no indication that the water table ever reached as high as the vault. All the sites in this area were much noisier at high frequencies than stations further north due to the presence of the low-velocity sediments and strong anthropogenic activity, which resulted in less usable data for these stations.

Data were acquired for a period of 1 yr, during which a total of 458 teleseismic earthquakes were recorded with suitable epicentral distances (20°–90°) and magnitudes greater than 5.2. Events with low quality signal are excluded, including small magnitude and distant events, low signal-to-noise ratio traces, and most aftershocks. The selection process keeps an average of 150 events per station. The selected three-component data are first rotated to the theoretical wave-arrival direction (backazimuth). After applying a bandpass filter between 0.05 and 2 Hz, deconvolution of the vertical trace from the radial and tangential ones is performed using the iterative time-domain method of Ligorria & Ammon (1999). The process is stopped after 50 iterations, or earlier if more than 95 per cent of the radial component signal is fit. Finally, we convolve the resulting spiky receiver functions with a Gaussian of a width corresponding to the maximum frequency (2 Hz).

3.1.2 Receiver function results

The obtained *P*-to-*S* radial receiver functions do not show significant variations with the backazimuth and are thus stacked at each station (Fig. 2). Moreover, the receiver functions calculated for the transverse component (not shown) do not show coherent energetic arrivals, which indicates the absence of both anisotropy and strongly
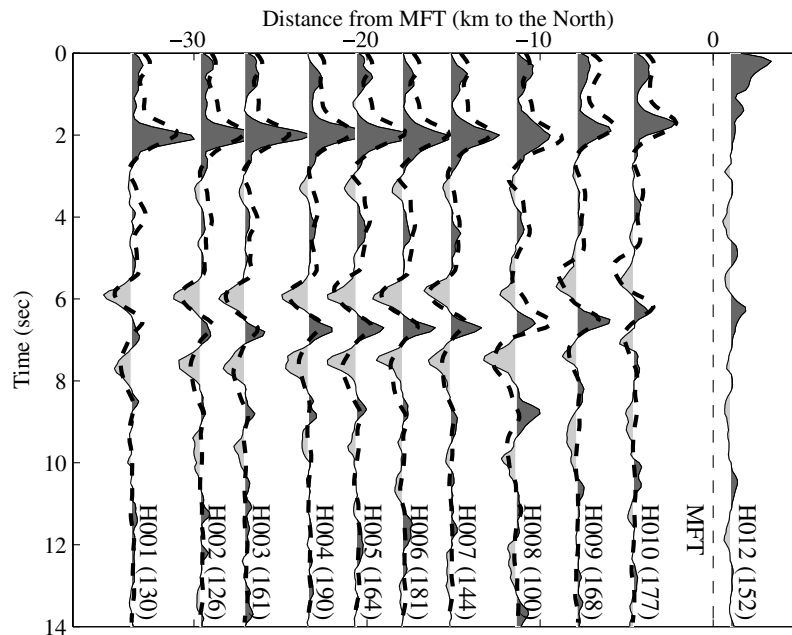
Figure 2. Stacked receiver function results (dark and light grey filled curves) in the Ganges basin. Station name is followed by the number of traces in stack (in parentheses). Superposed thicker dash lines at stations H001–H010 represent the average of 50 inverted traces at each station with the lowest misfit. Thin dashed line shows the location of the MFT.

dipping layers. We thus consider that the stacked radial receiver functions are representative of the structure beneath each station.

In general, the waveforms are similar between stations H001 and H010, all located in the Ganges basin. A common feature of these mean receiver functions is the lack of the *P*-wave arrival at 0 s, indicative of very low velocities close to the surface (e.g. Sheehan *et al.* 1995) that polarizes the direct *P*-wave almost vertically. The most energetic arrival is a prominent positive peak at around 2 s of delay compared to the *P*-wave reference time. Other coherent peaks on all traces are a negative–positive–negative sequence at around 6, 7 and 8 s, respectively, and secondary peaks at around 0.5–1 s delay. Small variations in arrival times and amplitudes can be observed along profile, such as the ∼10 per cent decrease in the amplitude of the 2 s-peak towards the north, or the ∼0.2 s earlier arrival of the 6–7–8 s sequence towards the north.

The waveform at station H012 is simpler compared to the others. This is mainly due to the fact that it is located right at the MFT, where the low-velocity alluvial layer is absent, and where the MFT brought more compacted, higher velocity sediments close to the surface (Lavé & Avouac 2000).

3.1.3 Waveform inversion procedure

In order to determine the detailed structure of the basin, we proceed to find velocity models that adequately match our observations at each station in the basin. This inverse problem being far from linear, we use the neighbourhood algorithm (NA; Sambridge 1999a), a stochastic inversion method based on partially guided exploration of the parameter space. Starting from a random distribution of parameter sets and establishing a rank of the corresponding cost functions, this method will preferentially sample the good data-fitting regions of the parameter space.

The application of the NA to the inversion of the receiver function problem is described by Sambridge (1999b), and we follow his procedure. Our process inverts traces for all 10 stations sepa-

rately, and iterations are stopped after 10 100 tested models. The best 50 models at each station are selected based on the lowest cost function values and are then averaged, as we ensure that they all belong to only one class of model.

An important question is the choice of the cost function. Mellman (1980) states that the best error-function in trying to match interacting waveforms is the L2-norm. However, as the L2-norm tries to minimize the difference between each time-sample, it is likely that secondary peaks with smaller amplitudes will be de-emphasized. Frederiksen (2000) proposes a cross-correlation based cost function, as it places less emphasis on amplitudes than on traveltimes, which are more robustly recovered features of receiver functions. The finally presented results in this study include two series of inversions, using one type of cost function each.

Our common starting model includes four layers: a thin low-velocity alluvial layer, a basin-filling sedimentary layer, crust, and mantle. It is clear that *a priori* information is necessary to better constrain the inversion results and to reduce the depth–velocity ambiguity, a common feature of receiver function non-uniqueness (Ammon *et al.* 1990). For this reason, the velocity of *P*-waves in the mantle is fixed to 8.1 km s^{-1} with a V$_P$/V$_S$-ratio of 1.85, and the crustal shear wave speed varies from 3.31 to 3.66 km s^{-1} from top to bottom with a V$_P$/V$_S$-ratio of 1.75. This value is consistent with previous estimates for the Indian crust (Kumar *et al.* 2001). As the porosities of the different Siwalik formations are different (Raiverman *et al.* 1983), we consider that the two upper layers are young enough that compaction may vary significantly with depth. Thus, we allow velocity to vary independently at the top and at the bottom of both layers, forming a linear velocity gradient. The remaining nine parameters to invert are summarized in Table 2.

3.1.4 Inversion results and interpretation

The inverted receiver function traces using the cross-correlation cost function at each station are represented in Fig. 2 (thick dashed lines).

Table 2. The nine parameters to invert with the Neighbourhood Algorithm with the allowed limits (based on *a priori* information).
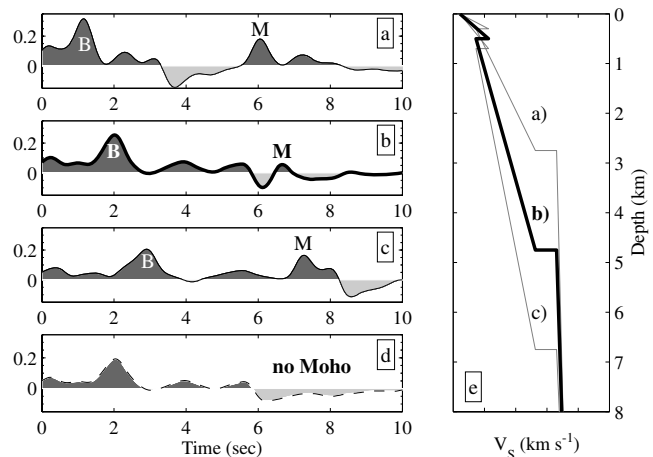
	Depth (km)	Velocity at the top (km s^{-1})	Velocity at the bottom (km s^{-1})	V_P/V_S ratio
Alluvial layer	0.2–1	0.2–1.3	0.2–1.3	1.75–2.3
Sedimentary layer	3–6.5	0.6–2.75	0.6–2.75	1.75–2.1
Crust	32–39	3.31 (fixed)	3.66 (fixed)	1.75 (fixed)
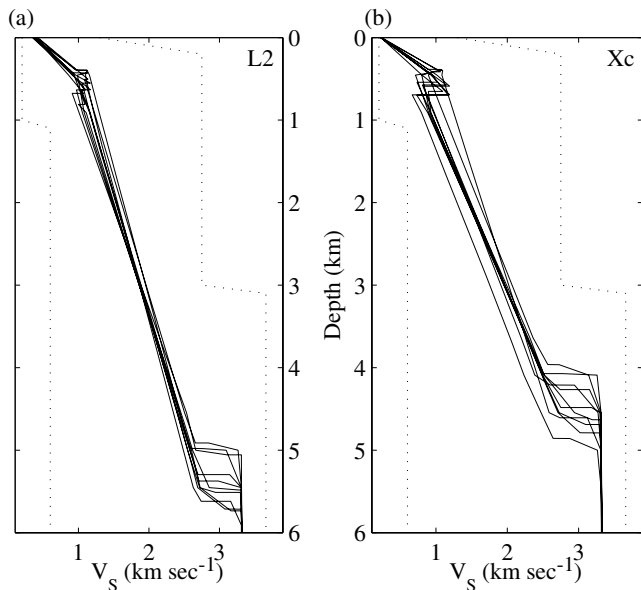
Figure 3. Inversion results for *S*-wave velocity in the sedimentary basin using a L2-norm (a) and a cross-correlation based error function (b). Each line represents the average of the 50 best velocity models at one station. Dotted lines are the allowed minima and maxima for the velocity values during inversion. The results show very low velocities in the alluvial layer, and a velocity-gradient in both the Siwaliks Group formation and the alluvial layer.

Figure 4. Synthetic receiver functions for sedimentary layers of different thickness, and the corresponding velocity models. (a)–(c): Comparison of receiver functions above a 2.75 km (a); a 4.75 km (b) and a 6.75 km; (c) deep basin. 'B' and 'M' give the arrival time of the *P*-to-*S* conversion at the base of the basin and at the Moho, respectively; (d) is the same as (b) except that there is no Moho in the model; (e) Velocity model. The alluvial layer's thickness is 0.5 km, and shear wave velocity is linearly increasing from 0.22 to 1.13 km s^{-1}. The velocity of the sedimentary layer increases from 0.73 to 2.63 km s^{-1}.

They reproduce properly both the arrival time and the amplitude of major peaks of the observed traces. However, secondary features are sometimes not as well reproduced. For example, the fit at station H008 is of lower quality probably because of less data available. Stations H001 to H010 represent very similar structural features. (Station H012, not inverted, makes an exception as it is located just above of the MFT). There is a slight difference between the profiles obtained with the two tested cost functions, which is that the cross-correlation method shows slightly shallower interfaces compared to the L2-norm.

The shear wave velocity–depth profiles in the basin obtained by both cost-function inversions are shown in Figs 3(a and b). All models show a very low speed of 0.2 km s^{-1} close to the surface, in the alluvial layer, which confirms the absence of a major peak at 0 s corresponding to the direct *P*-wave. This top layer exhibits very high V_P/V_S-ratio (~2.1), consistent with the unconsolidated nature of the sediments (Clitheroe *et al.* 2000), and a strong velocity gradient with depth of 1.3–1.55 s^{-1}, mainly due to the rapid compaction. The small velocity decrease at the base of the alluvial layer is not a robust feature of the NA-inversion results, and the amplitude of the corresponding negative receiver function peak is probably indistinguishable from noise.

The Siwaliks sedimentary layers show a mean velocity gradient of 0.3–0.45 s^{-1}, again consistent with an increase of compaction

and a decrease of porosity with depth, with an average V_P/V_S-ratio of 2. The interface corresponding to the base of the basin is imaged at a depth of 4.75 $\pm$ 0.25 km depending on the used cost function. It marks an important increase of *S*-wave velocity of 25 per cent, that produces a strong *P*-to-*S* conversion corresponding to the peak observed at ~2 s on the receiver functions. This interface also induces several high-amplitude reverberations inside the basin, such as the negative arrivals at ~6 and ~8 s.

Fig. 4 shows synthetic receiver functions that demonstrate the sensitivity of the waveform on basin depth. We have tested three basin depths (2.75, 4.75, 6.75 km) using the velocity variations obtained during the inversion (Fig. 4e) and keeping the crust–mantle boundary at 40 km depth. The synthetic receiver functions (Figs 4a–c) show how sensitive the arrival time of the *P*-to-*S* conversion at the base of the basin is to the depth of this interface: a shallower or a deeper basin is unambiguously incoherent with the observations, and the value of 4.75 km is preferred.

The Moho is recovered at a depth of 40 $\pm$ 0.5 km, depending on the cost-function. It corresponds to the positive peak seen on the receiver functions at ~7 s, as it is shown by the synthetic tests in Figs 4b and d. This depth value indicates that the thickness of the Indian crust, sediments excepted, is ~35 km. Beyond the effect of the cost-function, the 1σ standard deviation of the best 50 inverted models gives an uncertainty of $\pm$300 m and $\pm$1 km on the depth of the basin and of the Moho, respectively. Moreover, analyses of the spread of the selected models show that there is a small remaining
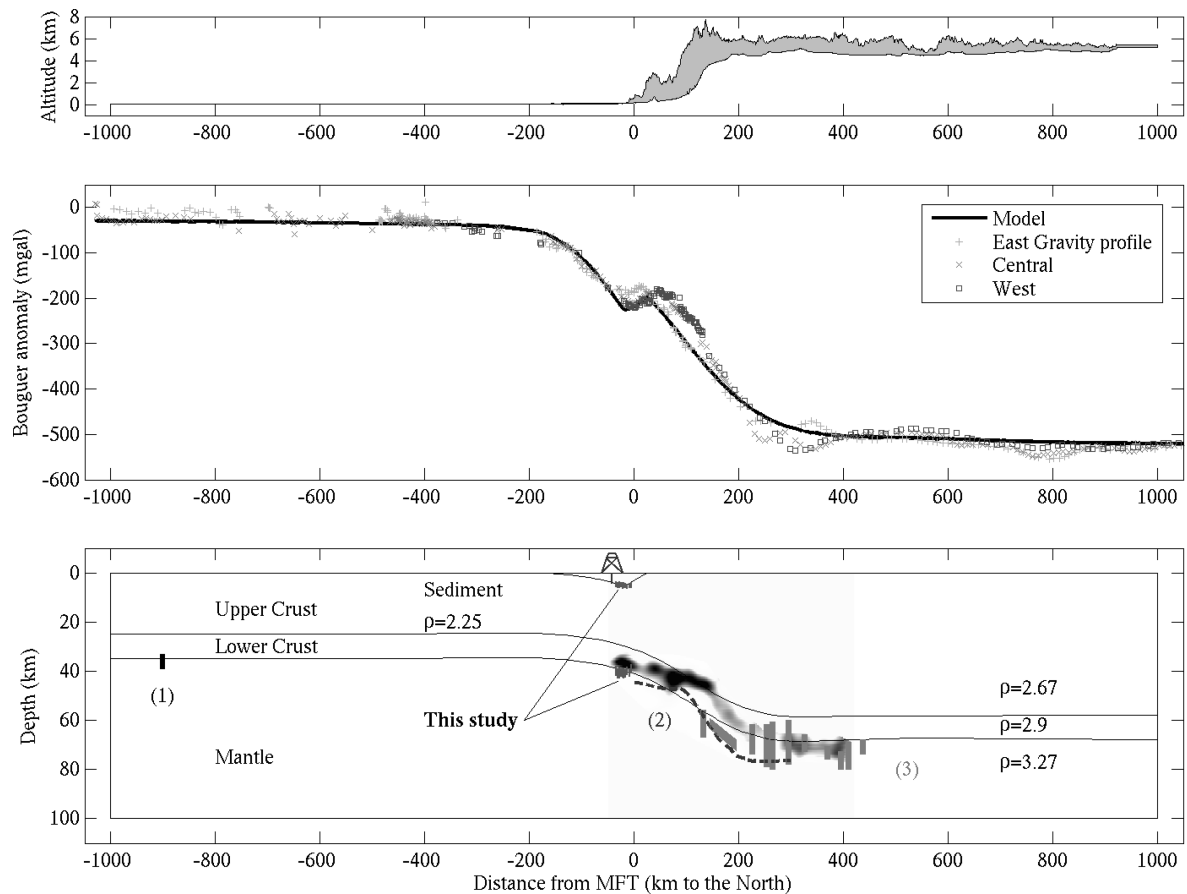
Figure 5. Data, model and results on a large scale profile. Top: minimum and maximum elevation averaged within 50 km on either side of the profile. Middle: data of the three gravity-measurement profiles (+, X, □ see Fig. 1 for location), and the calculated gravity anomaly (thick line). Bottom: the three-layer thermomechanical model with the sedimentary basin (densities are in g cm^{-3}). In grey, different geometrical constraints: sedimentary basin and Moho depth from receiver functions (error bars, this study); the Raxaul deep well's depth (Sastri *et al.* 1971); India Plate thickness from receiver functions (error bar (1), Kumar *et al.* 2001); Moho geometry (dashed line (2), Schulte-Pelkum *et al.*, 2005, depth datum is local surface elevation); Moho depth and dip of INDEPTH ((3) for receiver function error bars (Hauck *et al.* 1998) and Moho dip from migrated reflection profiles (Alsdorf *et al.* 1998), depth datum is sea level); and the shape of the Moho from receiver functions of the Hi-CLIMB experiment (background image patches, Nábělek *et al.* 2005 depth datumed is sea level). Results from other experiments were projected with reference to major thrust faults.

trade-off between the depth to an interface and the average velocity above it. All these uncertainties combined were taken into account for the geometrical constraints (Figs 5 and 7).

Inspection of the inversion results from south to north show that both the bottom of the basin and the Moho are subhorizontal, very gently dipping to the north. The estimated dip beneath this part of the basin is ∼0.7°. This value is smaller than all estimates obtained from previous studies, which suggests a rather rigid India Plate. This new image of the Ganges foreland basin and the underlying crust is used as a geometrical constraint in the following part of this paper.

3.2 Moho depth from Ganges basin to central Tibet

At larger scale, the main crustal structures have been described in detail by many authors (e.g. Hirn *et al.* 1984; Schelling & Arita 1991; Zhao *et al.* 1993; Avouac 2003). Here, we summarize the estimates of the Moho depth from the indo-gangetic plain to central Tibet, which is the main geometric constraint on the flexural behaviour of the India Plate. Kumar *et al.* (2001) give a 33–39 km thick crust for the south Indian shield from teleseismic receiver functions. This thickness is consistent with our estimate of

35 km beneath the Ganges basin. Our results on the Ganges basin, seismological experiment (Schulte-Pelkum *et al.* 2005) and gravity measurements (Cattin *et al.* 2001) all reveal that the Indian plate dips gently northwards. Both the HIMNT (Schulte-Pelkum *et al.* 2005) and the Hi-CLIMB (Nábělek *et al.* 2005) seismological experiments show a large deepening of the Moho beneath the front of the high Himalayas over a distance of 200–250 km, in agreement with the steep gradient of the Bouguer anomaly. In southern Tibet, all available seismological studies suggest a crustal thickness of the order of 70–80 km, consistent with isostatic support of the Tibetan plateau (Lyon-Caen & Molnar 1985; Cattin *et al.* 2001). All these features are summarized in the synthesis section shown in Fig. 5.

4 MODELLING THE FLEXURE

4.1 Thermomechanical modelling

Following Cattin *et al.* (2001), our model is based on a N18° cross-section perpendicular to the range, extending from India to the Tibetan plateau (Fig. 6). We use a 2-D finite element model (Hassani
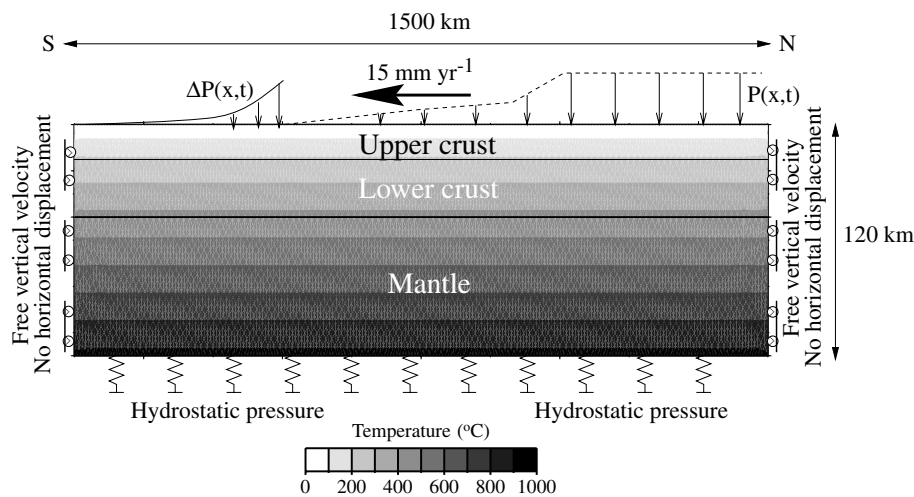
Figure 6. Initial stage of the thermomechanical model used in this study along a S-N profile. The mantle, the lower and upper crust are represented by three layers with different rheologies (Table 3). Vertical loads model the weight of the sediments (ΔP) and the crust Himalaya and Tibet (P). The load P moves southward at a rate of 15 mm yr^{-1} to simulate the Tibet–India convergence. Temperature varies with depth, and the gravitational force is 9.81 m s^{-2}. Free vertical displacements are allowed at both ends of the model, which is supported at its base by hydrostatic pressure. See text for more details.

et al. 1997) in a reference fixed to the India Plate. The Indian lithosphere is modelled by three bodies: the upper and lower crust and the mantle.

One of the main assumptions is that the model simulates the flexure of the India Plate only. Faults and mineral phase changes are not included. The load of the Himalayas, the Tibetan plateau and crust are modelled by a vertical pressure $P(x, t)$, proportional to the average elevation and crustal thickness along the profile, which excludes shear forces. The horizontal convergence rate of 15 mm yr^{-1} is simulated by the southward propagation of $P(x, t)$ with time. Similarly, the $\Delta P(x, t)$ accounts for the sedimentary infill of the foredeep. Sedimentation is assumed to maintain a flat foreland at a constant elevation (sea level) south of the MFT.

The model accounts for the mechanical layering of the crust and the non-Newtonian viscous rheology of rocks as a function of temperature and pressure. The rheologies are dependent on temperature, which is calculated from the Royden's (1993) formulation using a constant surface heat flow that corresponds to a reduced mantle heat flow of 15 mW m^{-2}, 273°K for the surface temperature and 2.5 μW m^{-3} for the upper crustal heat production. The entire model is submitted to gravitational forces ($g = 9.81$ m s^{-2}) and is supported at its base by hydrostatic pressure. Free vertical displacements are allowed at both ends of the model. Several tests, including model size, number of elements and time steps, are performed in order to avoid numerical instabilities related to the method and the boundary conditions, and to define characteristic parameters of our experiments. In further runs, the models have a length of 1500 km, include 9000 triangular elements, are ran for 10 Ma and each run is divided into 50 000 time steps.

During the exploration of the parameter space, 90 experiments are run altogether. The varied parameters are the following (between the limits shown in brackets): Young's modulus E [50–120 GPa], sediment density ρ_S [2250–2450 kg m^{-3}], crustal thickness Z_M [34–38 km], initial depth of the boundary between the upper and the lower crust (the Conrad discontinuity) Z_C [10–25 km], upper crustal density ρ_{UC} [2600–2900 kg m^{-3}] and Poisson's ratio ν [0.25–0.29] of the India Plate.

Some of the above parameters with very small influence on flexure geometry are fixed in the following, such as the upper crustal den-

Table 3. Rheological parameters used for a thermomechanical model with a strong mantle: ρ, density; ν, Poisson's ratio; c, cohesion; ϕ, internal friction angle; γ_0, power-law strain rate; n power-law exponent and E_a, power-law activation energy. For exact equations, we refer to Cattin *et al.* (2001). Material properties are from laboratory measurements. The values are taken from the compilation of Le Pichon & Chamot-Rooke (1991).

	Dry quartzite (upper crust)	Diabase (lower crust)	Wet dunite (upper mantle)
ρ (kg m^{-3})	2670	2900	3270
ν	0.25	0.25	0.25
c (MPa)	10	10	10
ϕ	30°	30°	30°
γ_0 (MPa^{-n} s^{-1})	1.585×10^7	6.31×10^2	398
n	2.9	3.05	4.5
E_a (kJ mol^{-1})	149	276	498

sity to 2670 kg m^{-3}, Poisson's ratio to 0.25 and crustal thickness to 35 km. Table 3 summarizes a set of rheological parameters used for a 'strong-mantle' model composed of quartz, diabase and dunite. 'Weak-mantle' type yield stress envelopes—with several rheologies similar to the ones in Jackson (2002)—are also used to test the flexural behaviour of this type of lithosphere, while keeping all other boundary conditions the same. The results of all these experiments are compared to geometrical constraints, such as-primarily-the geometry of the basin (Fig. 7), and-secondarily-the geometry of the Moho along the profile (Fig. 5).

4.2 Results and interpretation

4.2.1 Comparison with seismic images and limitations of the approach

The large number of performed test-runs shows that the geometry of the flexure is strongly influenced by the thickness of the upper crust, Z_C: the thicker it is, the smaller the curvature of the plate will be. This effect can be compensated or amplified by different sediment densities, Young's moduli, and by changing the rheology of the mantle. Geometrical constraints suggest a Young's modulus of
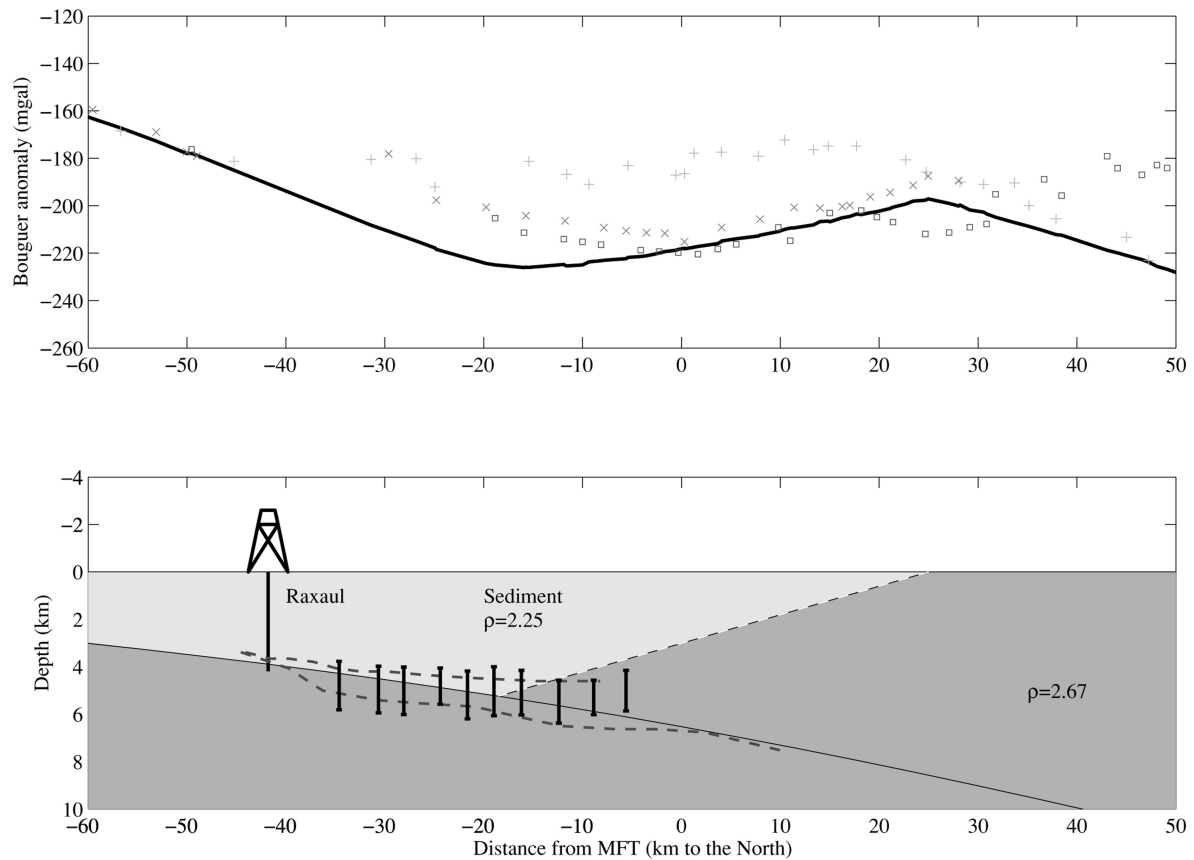
Figure 7. Data, model and results on a smaller scale profile. Top: measured and modelled small wavelength gravity anomaly (same legend as on Fig. 5). Bottom: flexural geometry of the final model with sedimentary infill (densities are in g cm^{-3}). The basin ends with a straight ramp (black-white dashed line) in order to take into account density variations. In black: depth extent of the Raxaul deep well (Sastri *et al.* 1971), base of the basin imaged by receiver functions (error bars, this study), and probable depth of the basin based on geological studies and seismic profiles (dashed lines; DMG 1990).

60–100 GPa, and we use $\rho_S = 2250$ kg m^{-3} for sediment density, a value most consistent with geological observations. Two end-members, with $Z_C = 15$ km and $Z_C = 25$ km will be analysed in more detail in the next section.

Considering the above influences, a set of dozen solutions was found to best fit the geometrical constraints, and their geometry is represented at both small (Fig. 7) and large scale (Fig. 5). We emphasize that the obtained geometries are the result of modelling flexural support of the topography only. The observations related to both faults and mineral phase changes (e.g. eclogitization) are not included, thus cannot be reproduced. For example, uplifted recent alluvial sediments south of the MFT suggest the presence of a blind thrust fault underneath the Ganges basin (Schelling 1992), which would slightly perturb the structure beneath stations H009 and H010, and thus explain the partly low quality fit of the model (Fig. 7). Other limitation of our modelling is being 2-D. Our calculations are consistent with data sets close to our study profile (gravity measurements, Hi-CLIMB profile, seismic reflection and the deep well data). However, our simple 2-D approach cannot reproduce lateral variations of the Moho shape imaged by the HIMNT and INDEPTH profile, which are 160 and 400 km away from our study profile, respectively.

4.2.2 Comparison with Bouguer anomaly

To validate the set of obtained solutions, we calculate the Bouguer anomaly associated to the final geometry of the modelled bodies,

including the Tibetan crust with a constant density of 2670 kg m^{-3}. The calculations are performed using the USGS Hypermag software (Saltus & Blakely 1995), which is based on the Ewing-Talwani line-integral method. The calculated anomalies are then compared to several gravity data sets merged (Cattin *et al.* 2001) to construct a 2000 km long profile, which is close to our seismological network (Fig. 1).

Figs 7 and 5 show the obtained geometries by numerical modelling, and the calculated Bouguer anomalies superposed to the observed data at both small (foreland basin) and large (from India to central Tibet) scales, respectively. At large wavelengths (Fig. 5), the calculated anomalies are in very good agreement with the measurements. As previously proposed by Cattin *et al.* (2001), we interpret the discrepancy observed at 300 km in term of eclogitization of the lowermost crust beneath southern Tibet. At a smaller scale (Fig. 7), our results are consistent with the general trend of the observations, showing a local minimum and maximum over a distance of ∼40 km. However, the residual gravity anomalies reveal two major disagreements: first, an offset of ∼15 km in horizontal distance, and second, a difference of ∼20 mGal in the amplitude. We interpret these disagreements as the joint effect of the followings.

(i) The oversimplified geometry used for the northern end of the Ganges basin. We kept the entire geometry issued from the numerical model and added only a straight line (black-white dashed ramp), to add the fewest parameters possible, to model the northern end of the basin.

(ii) Local density contrasts due to both compaction and lithological variations.

(iii) Lateral variations of the observations.

Such refined modelling, which requires to take into account geological features such as the MFT, MBT and Palung granites, is out of the scope of this paper. More detailed explanation of the gravity anomalies north of the foreland basin can be found in Cattin *et al.* (2001).

Despite these local discrepancies between observed and calculated Bouguer anomalies, our thermomechanical approach explains most of available geophysical data, and thus demonstrates the internal consistency of the used data sets and its compatibility with current understanding of the support of the topographic load in the Himalayan border of the Tibetan plateau.

4.2.3 Effective elastic thickness

The advantage of numerical thermomechanical modelling is an access to a great number of calculated physical parameters of the model, such as the effective viscosity

$$\eta = \frac{\sigma}{\dot{\varepsilon}}, \tag{1}$$

where σ and $\dot{\varepsilon}$ are stress and strain rate, respectively. We use this parameter to assess the EET in our depth-varying rheology models. For a plate decoupled into n layers, the EET is given by (e.g. Burov & Diament 1992)

$$EET = \left(\sum_{i=1}^{n} h_i^3 \right)^{1/3}, \tag{2}$$

where h_i is the elastic thickness of the ith layer. For each layer, h_i is the thickness of the elastic core, where relaxation time of the material is at least twice as long as the time of the experiment. The relaxation time τ is defined as

$$\tau = \frac{\eta}{E}, \tag{3}$$

with E being Young's modulus. The elastic part of a layer will be the region where η is larger than $\eta_{max} \sim 2\text{--}3.10^{25}$ Pa s for a modelled deformation age of 10 Ma and Young's modulus between 60 and 100 GPa.

Figs 8(a and b) show the effective viscosity profile with $Z_C = 15$ and 25 km, respectively. Both of these models are in agreement with the geometries of the data sets and with the earthquake distribution obtained by Maggi *et al.* (2000) and Chen & Yang (2004). This suggests that it is not possible to determine from geometrical constraints if there is intra-crustal coupling or decoupling within the central Indian shield. In both cases, the flexural rigidity of crustal layers decreases northwards due to thermal and flexural weakening, resulting in a very thin elastic core of the India Plate beneath the High Himalayas, and in no elastic core of the Indian crust beneath Tibet. In the mantle, even if the more viscous zone becomes thinner northwards, the uppermost mantle remains well above the threshold value η_{max}. The mean depth of the elastic core of the India Plate is about 80–85 km beneath the surface of the Tibetan plateau.

Fig. 9 gives the associated EET of the India Plate and the elastic thickness of each layer of the model along our study profile. Both cases show that there is a large decrease of the EET from south to north. In the south, beneath the central Indian Shield, the EET reaches a value as high as 70–80 km, which is consistent with its
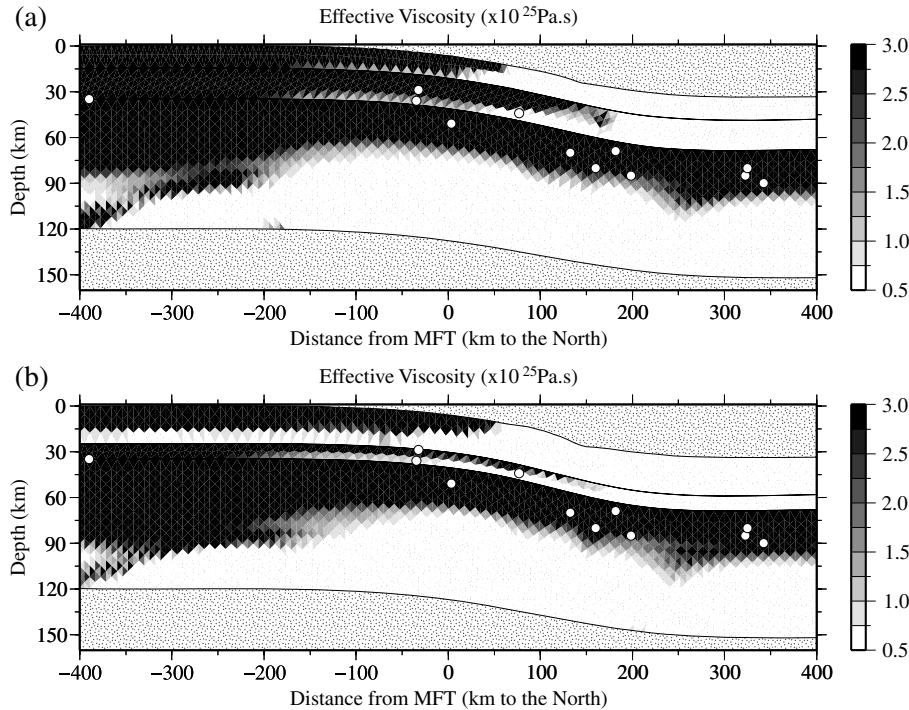

Figure 8. Effective viscosity profiles of the India Plate under a load simulating the Tibetan crust. (a) Completely coupled case under the Indian continent. (b) Decoupling at the upper crust–lower crust interface. White circles mark earthquakes discussed by Maggi *et al.* (2000) and by Chen & Yang (2004) as earthquakes occurring in the lower crust or in the upper mantle. Black areas are the strong, grey and white areas are the weak, ductile parts of the Indian lithosphere. In both cases, the mean depth of the elastic core of the India Plate is about 80–85 km beneath the Tibetan plateau. Lightly dotted areas, outside of the plate, are not modelled.
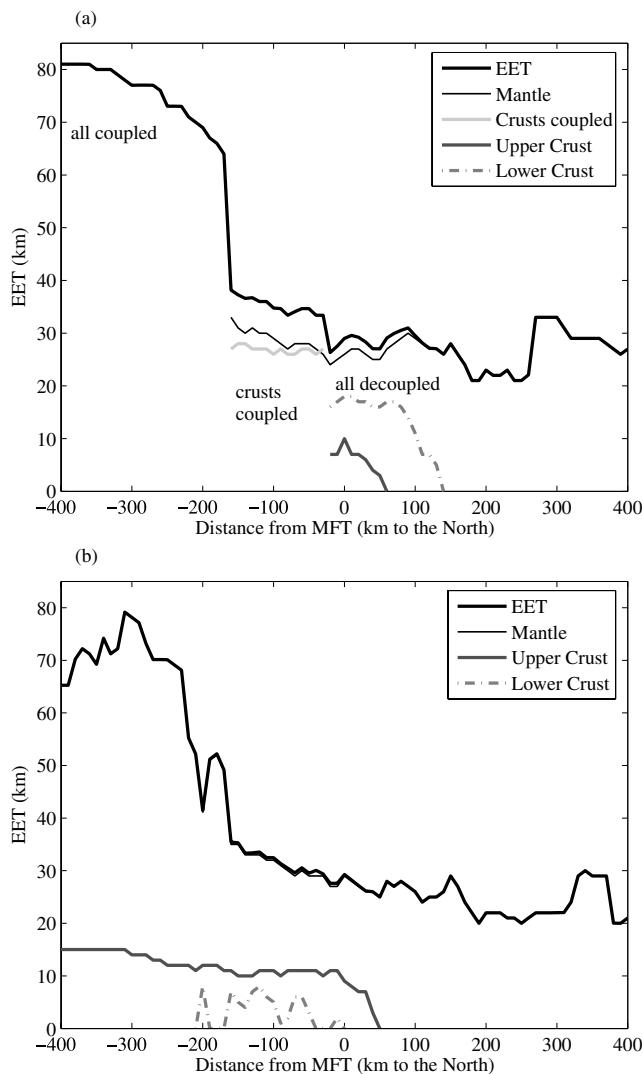
Figure 9. Effective elastic thickness of the different layers and of the entire Indian lithosphere, corresponding to Fig. 8(a) Completely coupled case under the Indian continent. Text inside the figure refers to ranges of distances with different coupling conditions between layers. (b) Decoupling at the upper crust–lower crust interface. In both cases, decoupling of the layers happens about 150–200 km south of the MFT, and the mantle remains the strongest part of the lithosphere north of this point.

thermotectonic age (Burov & Watts 2006). Decoupling of all layers from adjacent ones happens in a zone 200 km south of the MFT in both cases. Due to the cubic-mean employed in the calculation of the effective elastic thickness (eq. 2), this leads to a sudden drop of the EET, down to the 30–40 km range. It can also be seen that the elastic thickness of the mantle is larger than the crustal EET, even when the upper and lower crust are coupled. This reveals clearly the main role played by the upper mantle in the strength of the India Plate. North of the MFT, both the upper and lower crust loose their strength under the effect of flexure and temperature, while the elastic thickness of the mantle decreases only slightly. Here the EET of the Indian lithosphere ranges between 20 and 30 km, which is consistent with the value previously proposed by Jin *et al.* (1996). The main (and only) contribution to the strength of the Indian lithosphere comes from the mantle, as previously suggested by Lyon-Caen & Molnar (1983). This is true for all cases throughout the entire northern part

of the profile, under the Himalayas and the Tibetan plateau, which are thus mainly held up by a strong uppermost mantle. We note that if a real Tibetan crust was present in the model, or eclogitization could be modelled, the EET might have a higher value in this region, but the strength of the Indian upper mantle and its role would remain the same.

4.2.4 Comparison with previous studies

The new seismological constraints on Moho and basin depths, together with existing data, have been used to constrain the output of numerical models, which allowed us to re-estimate the EET of the India Plate from India to central Tibet. Here we discuss the difference of our results with previous studies.

Our EET-estimate is consistent with the first studies based on analytical solutions of the flexure of a 2-D thin plate under both the weight of topography and sediments and the effect of additional bending moments (Lyon-Caen & Molnar 1983; Jin *et al.* 1996) . The main difference compared to these studies is the better constraint on the depth of the basin, the modelling method (viscoelastoplastic behaviour, which includes thermal information, instead of elastic flexure with additional bending moment), and the larger amount of gravity-anomaly data used. As previously mentioned by Lyon-Caen & Molnar (1983), our results suggest a near-constant value of the EET in the region located ~150 km north of the MFT, and its low value is associated with the loss of the strength of the Indian crust beneath southern Tibet.

Our estimated EET value of 60–80 km in India and 20–30 km beneath the Tibetan plateau is also consistent with the recent result of Jordan & Watts (2005) and Burov & Watts (2006), which suggest an EET of 40–100 and 70 km, respectively. However, a detailed comparison of our results with a section of the EET-map of Jordan & Watts (2005) along our profile shows that their maximum value obtained is higher by 20–30 km, and that the drop in the value of the EET occurs further to the north. The method of Jordan & Watts (2005) has some difficulties resolving high EET-values based on gravity modelling, because there is little change in flexure and, hence, gravity anomaly for EET-values over ~70 km (Tony Watts, personal communication, 2006). As of the difference in the position of the EET-drop, the coupled or decoupled state of the lithospheric layers is very sensitive to the assumed rheology and thermal regime, which are the less well controlled parameters in our modelling. The use of a slightly colder regime and/or a more viscous rheology (e.g. more mafic composition of the lower crust) would cause coupling of the layers further north and, hence, a better agreement.

In contrast, our results do not agree with the estimates of McKenzie & Fairhead (1997) and Jackson (2002), who give a constant EET of ~40 km south of the MFT. Following Jackson (2002), we test several yield stress envelopes with a strong crust and a weak mantle using different viscous mantle and crustal rheologies in our thermomechanical modelling in order to check the 'weak-mantle' rheology. Most of the tests end with viscous or plastic instability, similarly to the results of Burov & Watts (2006). In the successfully finished tests, the obtained geometry is clearly inconsistent with the observations: the flexural geometry has its bulge at the location of the 4-km-deep sedimentary basin, meaning that the wavelength of the flexure is much smaller than the real case (Fig. 10). We draw the attention to the gravity anomaly profile presented in Jackson (2002), which does not extend north of the MFT, and so it ranges between +20 and −60 mGal only, excluding the larger amplitudes
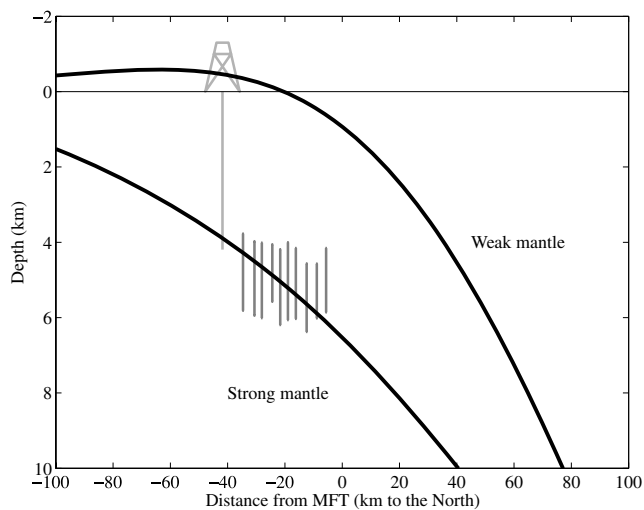
Figure 10. Flexural geometries obtained by 'strong-mantle' and 'weak-mantle' type rheologies. Dark grey error bars represent the base of the basin imaged by receiver functions (this study), light grey line shows the depth of the Raxaul deep well (Sastri *et al.* 1971).

(-550 mGal under Tibet in our profile). The limited extent of their profile may explain some of differences in the value of the EET. Moreover, our new seismological images of the Himalayan foreland suggest shallower structures than in earlier studies, so the re-assessed earthquakes of Maggi *et al.* (2000) have occurred in the mantle (Fig. 8a).

Cattin *et al.* (2001) have previously performed thermomechanical modelling in this region and found a lower EET of 40–50 km in the Himalayan foreland. The difference from their study to the present paper is the new seismological data that helps to constrain the depth and shape of the Moho as well as the geometry of the Ganges basin. Our re-evaluated Indian crustal thickness is 35 km, compared to the assumed 40 km in Cattin *et al.* (2001). The use of this lower value resulted in the coupling of the mantle and the lower crust south of the MFT in our study, while they were decoupled in Cattin *et al.* (2001), yielding lower EET-values of about 20–30 km.

4.2.5 *Dependence on relaxation time*

The main feature of the presented EET-profile across the Himalaya is the general northward weakening of the lithosphere, and the sudden drop of the EET at 150–200 km south of the MFT due to the decoupling of the crust and the mantle. This EET-profile was calculated using a constant relaxation time of 10 Ma. However, it is clear that age of the deformation is not constant along the profile: it can be as high as 50 Ma in the Himalayas, and as low as a couple of millions of years in the foreland, as it is suggested by the age of the sediments. Fig. 11 represents a smoothed EET-map as a function of distance from the MFT and characteristic relaxation time, for both the coupled and decoupled case. The previous calculation with a relaxation time of 10 Ma corresponds to the abscissa. In order to take account for the variable age of deformation along a transect perpendicular to the mountain range, oblique sections-such as the 20 or 50 mm yr^{-1} examples-should be considered. The use of these more realistic sections emphasizes the more important feature of the EET-profiles: a northward decrease from a value as high as 90 km to as low as 20 km is possible within a distance of 600 km. The transition is somewhat smoother in the coupled case (a) than in the decoupled one (b). This emphasizes the importance of the
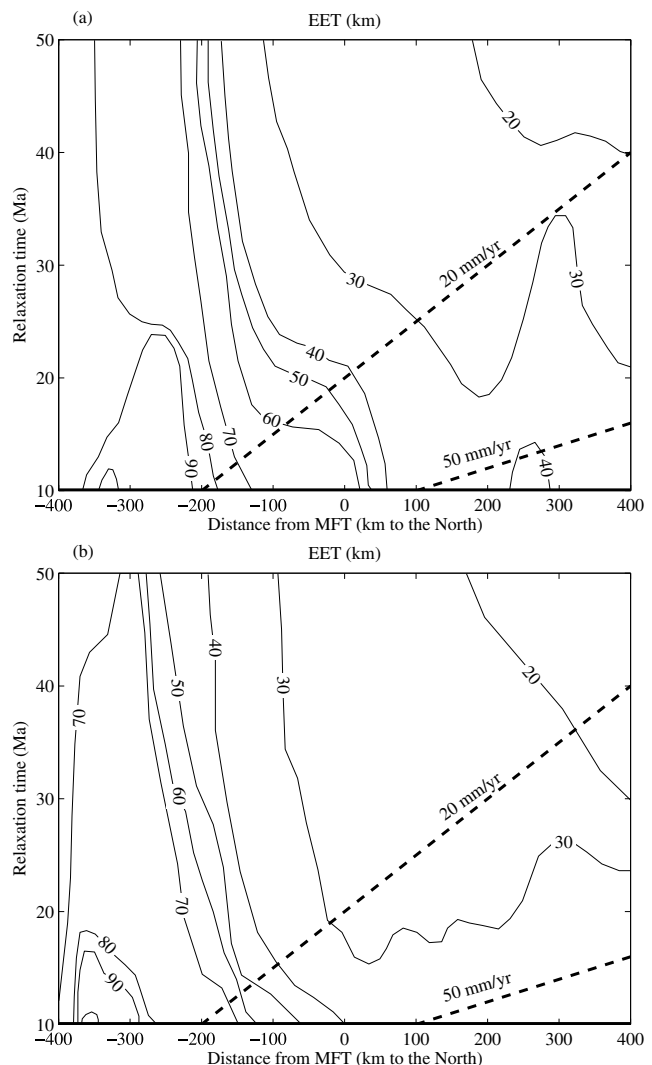

Figure 11. Map view of effective elastic thickness as a function of relaxation time and distance from the MFT. (a) and (b) represent the same cases as on Figs 8 and 9. The figures were drawn by calculating several EET-profiles with different effective viscosity threshold values corresponding to different deformation ages. The values on the abscissa (thick solid line), corresponding to 10 Ma of deformation age, are the values represented in Figs 8 and 9. An EET-profile associated to a higher deformation age is a section of this map along a horizontal line. Taking into account the difference in the age of the deformation under the Himalaya and of the foreland, oblique EET-profiles should be considered such as the dashed lines corresponding to different convergence rates. The main features of the EET-profiles (high values in the south, low values in the north) remain similar.

uncertainties on the estimated EET, which clearly depends on parameters still unconstrained as the rheology of both crust and upper mantle, the thickness of the upper crust or the detailed timing of the deformation across the Himalayas. Based on our set of numerical tests we estimate that EET values obtained in this study should be handled with a 5–10 km error bar.

5 CONCLUSIONS

We re-evaluate the EET of the India Plate by using new seismological data of the Hi-CLIMB experiment, and by determining the geometry of the interfaces beneath the Ganges basin. Depths to the base of

the sedimentary basin and to the Moho are found to be 5 and 40 km, respectively, with both interfaces dipping at a very shallow angle ($<1.5°$).

These, together with available geometrical constraints as well as the large-scale Hi-CLIMB image, are used in a three-layer thermomechanical model, in order to study the flexure of the Indian lithosphere. We simulate the effect of the Tibetan plateau using a vertical load. We neglect the effect of the EET of the Eurasian crust, associated with the elastic core of the upper and lower crust, and the decoupling of the shear zone, associated with the MHT. Thus, we favour a simple approach with no shear stress at the top of the India Plate.

Based on these assumptions, physical properties of the model then permit to calculate the effective elastic thickness along the entire profile. The results show that the EET of the India Plate:

(i) Is high under the Indian continent ($>60–70$ km) due to the coupling between crust and mantle.

(ii) Drops to a value of 30–40 km in a transitional zone at 150–200 km south of the MFT because of gradual decoupling.

(iii) Reaches a value as low as 20–30 km north of the MFT due to the loss of the crustal strength. The elastic core in this region resides in the mantle of the India Plate, which implies that it is the main support of the Himalayan-Tibetan load.

The characteristics of the obtained EET-profile are even more emphasized if we take into account the age of deformation of each region. The resulting geometry and the densities associated to the layers allow calculating the gravity anomalies along the same profile, which are consistent with the observed gravity anomalies.

The large disagreement in the value of the EET presented by earlier studies is probably due to the facts that either the model was too simple, either the data set did not cover the entire collision zone, or that the study was based on fewer types of data. Our results clearly show that rheologies with a weak mantle are not possible in this region, as the resulting flexural geometry is inconsistent with the observations.

ACKNOWLEDGMENTS

REFERENCES

Agocs, W.B., 1957. *Aeromagnetic survey of Indo-Gangetic Plains and Rajasthan*. Oil Nat. Gas. Comm., unpublished report.

Alsdorf, D. et al., 1998. INDEPTH (International Deep Profiling of Tibet and the Himalaya) multichannel seismic reflection data: description and availability. *J. geophys. Res.,* **103,** 26 993–26 999.

Ammon, C.J., 1991. The isolation of receiver effects from teleseismic P waveforms. *Bull. seism. Soc. Am.,* **81,** 2504–2510.

Ammon, C.J., Randall, G.E. & Zandt, G., 1990. On the non-uniqueness of receiver function inversions. *J. geophys. Res.,* **95,** 15 303–15 318.

Armijo, R., Tapponnier, P., Mercier, J.L. & Han, T.L., 1986. Quaternary extension in southern Tibet: field observations and tectonic implications. *J. geophys. Res.,* **91,** 13 803–13 872.

Avouac, J.-P., 2003. Mountain building, erosion, and the seismic cycle in the Nepal Himalaya. *Adv. Geophys.,* **46,** 1–80, doi:10.1016/S0065–2687(03)46001–9.

Burov, E. & Diament, M., 1992. Flexure of the continental lithosphere with multi-layered rheology. *Geophys. J. Int.,* **109,** 449–468.

Burov, E. & Diament, M., 1995. The effective elastic thickness (T_e) of continental lithosphere: What does it really mean? *J. geophys. Res.,* **100,** 3905–3928.

Burov, E.B. & Watts, A.B., 2006. The long-term strength of the continental lithosphere: 'jelly sandwich' or 'crème brûlée''? *GSA Today,* **16**(1), 4–10.

Cattin, R., Martelet, G., Henry, P., Avouac, J.-P., Diament, M. & Shakya, T.R., 2001. Gravity anomalies, crustal structure and thermomechanical support of the Himalaya of Central Nepal. *Geophys. J. Int.,* **147,** 381–392.

Chen, W.-P. & Yang, Z., 2004. Earthquakes Beneath the Himalayas and Tibet: Evidence for Strong Lithospheric Mantle. *Science,* **304,** 1949–1952.

Chen, Q., Freymueller, J.T., Wang, Q., Yang, Z., Xu, C. & Liu, J., 2004. A deforming block model for the present-day tectonics of Tibet. *J. geophys. Res.,* **109,** B01403, doi:10.1029/2002JB002151.

Clitheroe, G., Gudmundsson, O. & Kennett, B.L.N., 2000. Sedimentary and upper crustal structure of Australia from receiver functions. *Aust. J. earth Sci.,* **47,** 209–216.

DMG (1990). *Exploration Opportunities in Nepal*. Department of Mines and Geology, Kathmandu, 32 p.

Frederiksen, A.W., 2000. Seismic imaging of the Canadian upper mantle. *PhD thesis*, University of British Columbia.

Hassani, R., Jongmans, D. & Chéry, J., 1997. Study of plate deformation and stress in subduction processes using two-dimensional finite element models. *J. geophys. Res.,* **102,** 17 951–17 965.

Hauck, M.L., Nelson, K.D., Brown, L.D., Zhao, W. & Ross, A.R., 1998. Crustal structure of the Himalayan Orogen at approximately 90 degrees east longitude from Project INDEPTH deep reflection profiles. *Tectonics,* **17**(4), 481–500.

Hetényi, M., 1946. *Beams on Elastic Foundation*. University of Michigan Press, Ann Arbor, 255 p.

Hirn, A., Sapin, M., Lépine, J.C., Xu, Z.X., Gao, E.Y., Teng, J.W. & Pandey, M.R., 1984. Crustal structure and variability of the Himalayan border of Tibet. *Nature,* **307,** 23–25.

Jackson, J., 2002. Strength of the continental lithosphere: time to abandon the jelly sandwich? *GSA Today,* **12**(9), 4–10.

Jin, Y., McNutt, M.K. & Zhu, Y.S., 1996. Mapping the descent of the Indian and Eurasian plates beneath the Tibetan plateau from gravity anomalies. *J. geophys. Res.,* **101,** 11 275–11 290.

Jordan, T.A. & Watts, A.B., 2005. Gravity anomalies, flexure and the elastic thickness structure of the India-Eurasia collisional system. *Earth planet. Sci. Lett.,* **235,** 732–750.

Karner, G.D. & Watts, A.B., 1983. Gravity anomalies and flexure of the lithosphere at mountain ranges. *J. geophys. Res.,* **88,** 10 449–10 477.

Kumar, M.R., Saul, J., Sarkar, D., Kind, R. & Shukla, A.K., 2001. Crustal structure of the Indian Shield: New constraints from teleseismic receiver functions. *Geophys. Res. Lett.,* **28**(7), 1339–1342.

Langston, C., 1979. Structure under Mount Rainier, Washington, inferred from Teleseismic body-waves. *J. geophys. Res.,* **84**(B9), 4749–4762.

Larson, K.M., Bürgmann, R., Bilham, R. & Freymueller, J.T., 1999. Kinematics of the India–Eurasia collision zone from GPS measurements. *J. geophys. Res.,* **104**(B1), 1077–1093.

Lavé, J. & Avouac, J.P., 2000. Active folding of fluvial terraces across the Siwaliks Hills, Himalayas of central Nepal. *J. geophys. Res.,* **105,** 5735–5770.

Le Pichon, X. & Chamot-Rooke, N., 1991. Extension of the continental crust. in *Controversies in Modern Geology: Evolution of Geological Theories in Sedimentology, Earth History and Tectonics,* eds Müller, D.W., McKenzie, J.A. & Weissert, H., academic press, London, 313–338.

Ligorria, J. & Ammon, C.J., 1999. Iterative deconvolution and receiver–function estimation. *Bull. seism. Soc. Am.,* **89**(5), 1395–1400.

Lyon-Caen, H. & Molnar, P., 1983. Constraints on the structure of the Himalaya from an analysis of gravity anomalies and a flexural model of the lithosphere. *J. geophys. Res.,* **88**(B10), 8171–8191.

Lyon-Caen, H. & Molnar, P., 1985. Gravity anomalies, flexure of the Indian plate and the structure, support and evolution of the Himalaya and Ganga Basin. *Tectonics,* **4,** 513–538.

Maggi, A., Jackson, J.A., Priestley, K. & Baker, C., 2000. A re-assessment of focal depth distributions in southern Iran, the Tien Shan and northern India: do earthquakes really occur in the continental mantle? *Geophys. J. Int.,* **143,** 629–661.

McKenzie, D. & Fairhead, D., 1997. Estimates of the effective elastic thickness of the continental lithosphere from Bouguer and free air gravity anomalies. *J. geophys. Res.,* **102**(B12), 27 523–27 552.

Mellman, G., 1980. A method of body–wave waveform inversion for determination of Earth structure. *Geophys. J.R. Astron. Soc.,* **62,** 481–504.

Métivier, F., Gaudemer, Y., Tapponnier, P. & Klein, M., 1999. Mass accumulation rates in Asia during the Cenozoic. *Geophys. J. Int.,* **137,** 280–318.

Nábělek, J.L., Vergne, J. & Hetényi, G., 2005. Project Hi-CLIMB: A synoptic view of the Himalayan collision zone and Southern Tibet, EoS Trans. AGU, **86**(52), Fall Meet. Suppl., Abstract T52A-02.

Nelson, K.D. *et al.,* 1996. Partially molten middle crust beneath southern Tibet: synthesis of project INDEPTH results. *Science,* **274,** 1684–1688.

Raiverman, V., Kunte, S.V. & Mukherjea, A., 1983. Basin geometry, Cenozoic sedimentation and hydrocarbon prospects in north western Himalaya and Indo-Gangetic Plains. *Petrol. Asia J.,* **11,** 67–92.

Royden, L.H., 1993. The steady-state thermal structure of eroding orogenic belts and accretionary prisms. *J. geophys. Res.,* **98,** 4487–4507.

Saltus, R.W. & Blakely, R.J., 1995. HYPERMAG: An interactive, 2- and 2.5-dimensional gravity and magnetic modelling program, version 3.5. US Geological Survey Open-File Report 93-287, Reston, VA, 39 pp.

Sambridge, M., 1999a. Geophysical inversion with a neighbourhood algorithm – I. Searching a parameter space. *Geophys. J. Int.,* **138,** 479–494.

Sambridge, M., 1999b. Geophysical inversion with a neighbourhood algorithm – II. Appraising the ensemble. *Geophys. J. Int.,* **138,** 727–746.

Sastri, V.V., Bhandari, L.L., Raju, A.T.R. & Datta, A.K., 1971. Tectonic framework and subsurface stratigraphy of the Ganga basin. *J. Geol. Soc. India,* **12**(3), 222–233.

Schelling, D., 1992. The tectonostratigraphy and structure of the eastern Nepal Himalaya. *Tectonics,* **11**(5), 925–943.

Schelling, D. & Arita, K., 1991. Thrust tectonics, crustal shortening, and the structure of the far–eastern Nepal Himalaya. *Tectonics,* **10**(5), 851–862.

Schulte-Pelkum, V., Monsalve, G., Sheehan, A., Pandey, M.R., Sapkota, S., Bilham, R. & Wu, F., 2005. Imaging the Indian Subcontinent beneath the Himalaya. *Nature,* **435,** 1222–1225.

Sheehan, A.F., Abers, G.A., Jones, C.H. & Lerner-Lam, A.L., 1995. Crustal thickness variations across the Colorado Rocky Mountains from teleseismic receiver functions. *J. geophys. Res.,* **100,** 20 391–20 404.

Watts, A.B. & Zhong, S., 2000. Observations of flexure and the rheology of oceanic lithosphere. *Geophys. J. Int.,* **142,** 855–875.

Watts, A.B. & Burov, E.B., 2003. Lithospheric strength and its relationship to the elastic and seismogenic layer thickness. *Earth planet. Sci. Lett.,* **213,** 113–131.

Wilson, C.K., Jones, C.H. & Gilbert, H.J., 2003. Single-chamber silicic magma system inferred from shear wave discontinuities of the crust and uppermost mantle, Coso geothermal area, California. *J. geophys. Res.,* **108**(B5), 2226, doi:10.129/2002JB001798.

Zhao, W., Nelson, K.D. & Project INDEPTH Team (1993). Deep seismic reflection evidence for continental underthrusting beneath southern Tibet. *Nature,* **366,** 557–559.

Zheng, T., Zhao, L. & Chen, L., 2005. A detailed receiver function image of the sedimentary structure in the Bohai Bay Basin. *Phys. Earth planet. Inter.,* **152,** 129–143, doi:10.1016/j.pepi.2005.06.011.